A novel thermal-tuning Fe-based amorphous alloy for automatically recycled methylene blue degradation

Weiming Yang [a], Qianqian Wang [b,1], Wenyu Li [a], Lin Xue [b], Haishun Liu [a,*], Jing Zhou [b], Jinyong Mo [a], Baolong Shen [a,b,**]

[a] State Key Laboratory for Geomechanics and Deep Underground Engineering, School of Mechanics and Civil Engineering, Institute of Massive Amorphous Metal Science, China University of Mining and Technology, Xuzhou 221116, People's Republic of China
[b] School of Materials Science and Engineering, Jiangsu Key Laboratory for Advanced Metallic Materials, Southeast University, Nanjing 211189, People's Republic of China

HIGHLIGHTS

- $Fe_{63}Cr_5Nb_4Y_6B_{22}$ amorphous ribbon with good catalytic ability in Fenton-like reaction was synthesized.
- An automatically recycled dye degradation system was designed based on $Fe_{63}Cr_5Nb_4Y_6B_{22}$ amorphous ribbons.
- The good catalytic property of $Fe_{63}Cr_5Nb_4Y_6B_{22}$ amorphous ribbons are attributed to their local heterogeneous structures.

GRAPHICAL ABSTRACT
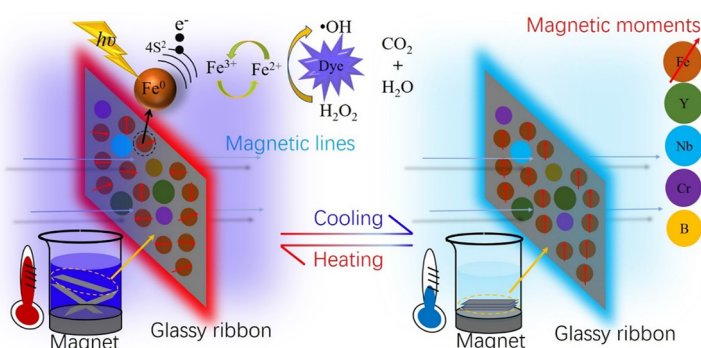
ARTICLE INFO

ABSTRACT

The comprehensive utilization of the excellent magnetic properties and advanced catalytic ability of Fe-based amorphous alloys (FAAs) is reported for the first time. A novel $Fe_{63}Cr_5Nb_4Y_6B_{22}$ (at%) amorphous alloy that has ferromagnetic to paramagnetic transition near room temperature and good catalytic performance for methylene blue degradation is successfully synthesized. The alloy is applicable for automatically recycled dye degradation with its thermal-tuning magnetic behavior. When an external dye wastewater is applied (high temperature), the FAAs are paramagnetic and disperse into water to participate in degradation. When the wastewater has been degraded and the temperature drops to room temperature, the FAAs change to ferromagnetic and the remediated water can be released. This alloy exhibits a low thermal activation energy barrier of 21.8 kJ/mol due to the reduced atomic bonding forces with Cr addition, and has excellent catalytic performance at high temperature (323–343 K) and in acidic solution (pH = 3). The excellent chemical properties are mainly attributed to the heterogeneous structure consisting of local Fe-rich and Fe-poor atomic clusters. The present findings not only provide a new, highly efficient and low cost commercial method for wastewater treatments, but also shed light on the comprehensive utilization of the magnetic and chemical properties of FAAs.

* Corresponding author.
** Correspondence to: B. Shen, School of Materials Science and Engineering, Jiangsu Key Laboratory for Advanced Metallic Materials, Southeast University, Nanjing 211189, People's Republic of China
   E-mail addresses: liuhaishun@cumt.edu.cn, liuhaishun@126.com (H. Liu), blshen@seu.edu.cn (B. Shen).
[1] Contributes equally with the first author.

1. Introduction

Textile industry consumes a large volume of water and different kinds of chemicals during the wetting process, which causes not only environmental but also ecological problems if not well treated before discharging. Among all the chemicals, dyes are highly visible even with very low concentration, and have potential carcinogenicity and teratogenicity [1,2]. Besides, most dyes can't be decomposed by the aerobic organisms in nature as they are chemically stable [3,4]. Thus, exploration of the high-efficient treatment of dye wastewater is one of the most important subjects in pollution controls.

Advanced oxidation processes (AOP) are effective methods to remove organic compounds and microorganisms from polluted water by generating oxidative radicals [5–9]. The high degradation efficiency, low materials cost and sustainability of AOP guarantees them wide application potential in wastewater remediation. The Fenton reaction is one of the widely used AOPs to remediate toxic components in the aqueous matrix through activating the hydrogen peroxide to produce highly reactive transitory species [10–12]. However, the Fe ions/salts used as the catalysts in homogeneous Fenton reaction lead to some disturbance to the industrialization of this technology: (i) ferric hydroxide sludge is easily produced in alkaline conditions, which brings in the cost associated with the purification of the secondary sludge and blocks the UV radiation penetration in photo-Fenton method [13]; (ii) the iron ions are difficult to be recycled and reused [14]. To overcome these shortcomings, zero-valent iron (ZVI) with various dimensions, commonly in granular/powder form or as nanoscale particles, are employed instead of Fe ions [15]. However, the large specific surface area of ZVI particles not only has positive impact as it enhances the generation rate of oxidative radicals to accelerate the dye decolorization during the Fenton process, but also brings negative effect on the storage and transportation of materials due to their low stability and corrosion resistance in air, especially in salted and humid atmosphere [3].

Recently, amorphous alloys, especially FAAs produced through rapid quenching, which successfully solidify the zero-valent state of iron in the obtained alloy, have been proved to have excellent performance in degrading dyes and other organic toxicants in wastewater [16–19]. Due to the short-range ordered and long-range disordered atomic structure, the metastable FAAs have high reactivity and large amounts of active sites on the surface, thus possess superiority in chemical property over traditional ZVI [20–23]. Several FAAs, including Fe-B [24], Fe-Si-B [25,26], Fe-Mo-Si-B [27], Fe-Si-B-Cu-Nb [28–30] and Fe-P-C [31] alloys have been reported to have advanced degrading/catalytic capability and satisfying reusability for wastewater remediation. The Fe-Si-B-Y powders in amorphous state presented 1000 times higher reactivity than the commercial Fe powders for methyl orange degradation, and the reusability of this alloy achieved 13 cycles [32]. The Fe-Si-B metallic glasses exhibited good reusability of 30 times and superior surface stability when activating persulfate for MB degradation [33]. The superior soft magnetic properties of FAAs make the recycling of the alloys after degradation reactions possible, and the chemical stability brings an acceptable level of surface decay and convenience for storage and transportation, both of which would lead to dramatic cost reductions [28]. Besides, the FAAs with unique mechanical and soft magnetic properties have been widely used as electronic and magnetic materials and massively produced in an industrial scale (in tons) by melt-spinning, providing a mature and stable product supply for actual industrialization of novel degradation processes [34].

However, there is still a big gap between laboratory researches and actual applications of FAAs for wastewater treatment due to several unsolved problems. Firstly, although the high temperature (around 323 K) of the wastewater effluents accelerates the degradation process [31], it also decreases the chemical stability of most FAAs, which reduces their service life. Secondly, the magnetic properties of FAAs have side impacts during the degradation process, including: (i) FAAs ribbons and/or powders easily aggregate when the electromagnetic stirring is applied; (ii) the magnetically collected ribbons/powders after each degradation cycle don't disperse into the wastewater batch automatically due to the residual magnetism. The exploration of a specific FAA with thermal-tuned magnetic properties may solve these problems.

The magnetic transition temperature, which is also called Curie temperature (T_C), is a unique characteristic for magnetic materials. At T_C, magnetic materials go through a reversible change from ferromagnetic to paramagnetic. The design of a degradation system using FAAs with a T_C below 323 K could be a solution for the two problems discussed above. It was revealed that the introduction of the antiferromagnetic metals (such as Cr) can effectively tune the magnetic properties and enhance the chemical stability of FAAs [35–37]. Thus, the design of an automatically recycled dye degradation system using thermal-tuning FAAs with good chemical stability by Cr addition is possible. Besides, although the applications of FAAs in degrading dyes/hazardous organics, or in magnetic devices have been widely studied, the design of a wastewater treatment system using both the degrading and magnetic properties has rarely been reported.

In this work, a novel Cr containing FAA with a T_C near room temperature and the high dye degradation efficiency is synthesized by minor addition of Cr in the Fe-B-Y-Nb system, which has the largest glass-forming ability in the FAAs with soft magnetic properties [38]. An automatically recycled system for dye degradation using the thermal-tuning Fe-Cr-B-Y-Nb amorphous ribbons as catalysis is designed: when the container is filled with high-temperature wastewater effluents, the FAAs become paramagnetic and disperse into the water for degradation; when the remediation of the wastewater is finished and the temperature decreases, the FAAs recover to ferromagnetic and can be easily collected by a permanent magnet; then the treated water can be discharged. Methylene blue (MB), $C_{16}H_{18}ClN_3S \cdot 3H_2O$, which is one of the typical synthetic dyes being utilized in biology and medicine as a photo chromophore to sensitize gelatinous films, is used as the target dye for degradation in this work [39]. The versatility, simple design, unique operating mode and high efficiency of the thermal-tuning material suggests that the Fe-Cr-Nb-Y-B amorphous alloy not only is a promising material to be used in the treatment of dye wastewater, but also has potential for thermal switches and thermal management solutions. This work takes advantages of the advanced magnetic and degrading properties of FAAs simultaneously for the first time, which should shed light on the comprehensive utilization of the physical and chemical properties of FAAs.

2. Experimental

2.1. Materials and reagents

Alloy ingots with nominal compositions of $Fe_{68-x}Cr_xNb_4Y_6B_{22}$ (x = 1, 3, 5, 7, and 9 at%) were prepared by arc melting a mixture of pure Fe, Cr, Nb, Y metals, and pure B crystal in a high-purity argon atmosphere, which was vacuumed to 5×10^{-3} Pa first and then filled with purified argon (99.999%). Each ingot was melted for 3 times to ensure its chemical homogeneity. Ribbons with a thickness of ~25 μm and a width of ~2 mm were prepared in a single roller melt-spinning system, which was vacuumed to 5×10^{-3} Pa first and then filled with purified argon (99.999%). The ribbons were obtained when the roller speed was about 40 m/s. The ribbons were cut into ~1 cm long for degradation experiments. Commercially available synthetic dye (Methylene blue, AR grade) was purchased from Xiya Reagent. Sodium hydroxide (NaOH, AR grade) was purchased from Greagent. Sulphuric acid (H_2SO_4, AR grade) was purchased from Chron Chemicals. Hydrogen peroxide (H_2O_2, AR grade) was purchased from Sinopharm Chemical Reagent Co., Ltd.

2.2. Characterization

The amorphous nature of as-quenched ribbons was verified by X-ray diffraction (XRD, Bruker D8 Discover) with Cu-Kα radiation and differential scanning calorimetry (DSC, NETZSCH DSC 404 F3) with a heating rate of 0.67 K/s. The thermal magnetic transitions of the as-quenched ribbons were measured by a physical property measurement system (PPMS, Quantum Design Model-9) at a heating/cooling rate of 0.167 K/s. For magnetic properties investigation, *M-H* hysteresis loops were measured with a vibrating sample magnetometer (VSM, Lake Shore 7407) at ambient temperatures. The density of the specimens was measured using Archimedes' method with the deviation <1%. For microstructure analysis, the ribbons were thinned carefully by a low-angle (5°) ion milling (GATAN-691) and then examined with high resolution transmission electron microscope (TEM, FEI Tecnai G2 F20). FTIR spectra of the melt-spun and after-degradation $Fe_{63}Cr_5Nb_4Y_6B_{22}$ ribbons were recorded on a FTIR spectrometer (Nicolet iS10, Thermo Scientific) with the baseline subtracted. Raman spectra of the melt-spun and after-degradation $Fe_{63}Cr_5Nb_4Y_6B_{22}$ ribbons were recorded on a Raman Microscope (LabRAM HR UV–Visible, Horiba Jobin Yvon). The ribbons for FTIR and Raman analyses were washed using DI water and dried in air before measurements.

2.3. Electrochemical tests

The electrochemical properties were analyzed using an electrochemical measuring instrument (Gamry Interface 1000). The measurement was conducted in a three-electrode cell using a platinum counter electrode and an Ag/AgCl reference electrode. The potential-dynamic polarization curves were recorded at a potential sweep speed at 4 mV/s after the open circuit potentials was stabilized. The solution used for the polarization measurements was 50 ml acid MB solution with H_2O_2 (pH = 3, 1 mM H_2O_2, 100 mg L^{-1} MB).

2.4. Degradation experiments

250 ml MB solution (100 mg L^{-1} if not noted) was prepared using deionized (DI) water in a 500 ml beaker. A specific amount of ribbons (0.5 g L^{-1} if not noted) and H_2O_2 (2 mM if not noted) were added into the solution, which was mechanically stirred at 400 r/min during the degradation process. Temperature of the solution was maintained using a water bath. The initial pH (pH = 3 if not noted) of the solution was adjusted using 5 vol% H_2SO_4, as well as 1 M and 0.1 M NaOH. At selected time intervals, 2.5 mL solution was extracted using a syringe and filtered with a 0.22 mm membrane, then scanned using a UV–vis spectrophotometer (Shimadzu UV-1280) to obtain the absorbance spectrum of the solution. For cyclic tests, the ribbons were extracted from the solution after each degradation experiment and stir washed using DI water for 20 s before put into the next reaction batch.

3. Results and discussion

3.1. Thermal stability and magnetic properties

3.1.1. Amorphous nature and thermal stability of the ribbons

Fig. 1(a) shows the XRD patterns of the melt-spun $Fe_{68-x}Cr_xNb_4Y_6B_{22}$ (x = 1, 3, 5, 7, and 9 at%) amorphous ribbons. As each pattern contains only broad maxima without any sharp Bragg peak showing traces of crystallites, the amorphous nature of all the samples can be confirmed. The TEM images also indicated the $Fe_{63}Cr_5Nb_4Y_6B_{22}$ ribbons synthesized in this work are fully amorphous before and after degrading reactions (Fig. S1 in Supplementary materials). It is found that the diffraction angle of the principal diffusive peak in XRD pattern doesn't change with Cr content. The short-range order (SRO) of amorphous alloys is related to the first coordination shell r_1, which corresponds to the position of the X-ray halo maximum according to the Bragg equation. Based on the

XRD results, the SRO of the obtained $Fe_{68-x}Cr_xNb_4Y_6B_{22}$ amorphous alloys doesn't change with the substitution of Cr for Fe, which is reasonable as the radius of Cr and Fe atoms are almost the same, being 0.128 nm and 0.126 nm, respectively [40]. Fig. 1(b) shows the DSC curves of the melt-spun $Fe_{68-x}Cr_xNb_4Y_6B_{22}$ amorphous ribbons. Each of the DSC curves of the alloys exhibits a distinct glass transition, followed by a supercooled liquid region and then crystallization. With the Cr content increasing from 1 to 9 at%, T_g increases gradually from 931 to 952 K, while T_x decreases from 999 to 979 K, leading to a decrease in ΔT_x from 68 to 27 K. As the heat of mixing of Cr-Nb pair (−7 kJ/mol) and Cr-Y pair (+11 kJ/mol) are larger than that of Fe-Nb pair (−16 kJ/mol) and Fe-Y pair (−1 kJ/mol), respectively [41], the bonding forces among the constituent elements in the alloys are reduced by partially replacing Fe with Cr, which results in the decreased thermal stability of the supercooled liquid.

3.1.2. Magnetic properties of the ribbons

The magnetic properties of the obtained $Fe_{68-x}Cr_xNb_4Y_6B_{22}$ (x = 1, 3, 5, 7, and 9 at%) amorphous alloys were thoroughly investigated under different temperature and applied magnetic fields. The effect of Cr addition on the T_C of melt-spun $Fe_{68-x}Cr_xNb_4Y_6B_{22}$ amorphous ribbons was examined by measuring the temperature dependence of the magnetization (*M-T* curves) at a heating/cooling rate of 0.167 K/s under a low magnetic field of 0.01 T, as shown in Fig. 1(c). The T_C, which is the temperature corresponding to the minimum of the d*M*/d*T* versus *T* curves, shifts toward lower temperature with the increasing of Cr content. The T_C for the 1 at% Cr alloy is 388 K and drops remarkably to 266 K by replacing 9 at% Fe with Cr. The drop of T_C can be explained by the antiferromagnetic exchange interaction between Fe and Cr atoms in amorphous alloys [42]. The T_C values of the amorphous alloys with 3, 5, and 7 at% Cr are 346, 300, and 266 K, all of which are near room temperature. Thus, $Fe_{68-x}Cr_xNb_4Y_6B_{22}$ amorphous alloys with T_C near room temperature have been successfully prepared by 3–7 at.% Cr addition.

In order to further verify the magnetic properties of the $Fe_{68-x}Cr_xNb_4Y_6B_{22}$ amorphous alloys near room temperature, their *M-H* hysteresis loops with different Cr contents were measured at 283 K, as shown in Fig. 1(d). The magnetization was calculated by using the actual density of the obtained mother ingots. With Cr content increasing from 1 to 5 at%, the alloys are preserved to be ferromagnetic although the saturation magnetization decreases monotonically from ~1.0 T to 0.25 T. When the Cr content is >5 at%, the alloys turn to be paramagnetic at 283 K. The results derived from the *M-T* and *M-H* curves confirm that the remarkable magnetism transition from ferromagnetic to paramagnetic near room temperature of $Fe_{68-x}Cr_xNb_4Y_6B_{22}$ alloys can be realized with 5–7% Cr addition. Taking the thermal stability, materials cost and thermal-magnetic behavior of the amorphous alloys into account simultaneously, the optimized composition of the $Fe_{68-x}Cr_xNb_4Y_6B_{22}$ alloys is obtained when Cr content is 5 at%. These specific thermal-magnetic properties make these alloys highly applicable as thermal-tuning materials.

3.1.3. Reliability and sensitivity and of the thermal-tuning magnetic alloy

The working principles of the thermal-tuning magnetic materials can be readily observed by measuring the magnetization of the alloys with designed cyclic thermal conditions under an applied constant field. Fig. 2(a) shows the magnetic evolution with heating and cooling cycles at low fields (0.02 T) for $Fe_{63}Cr_5Nb_4Y_6B_{22}$ alloy. During heating process, the magnetization of the alloy decreases rapidly from 35 emu/g to 0 emu/g when the temperature increases from 250 K to 300 K, and stays at 0 emu/g from 300 K to 400 K. During cooling process, the magnetization stays at 0 emu/g from 400 K to 300 K, then increases sharply from 0 emu/g to 35 emu/g when the temperature decreases from 300 K to 250 K. The maximum magnetization change is about 35 emu/g, without any reduction even after 5 cycles, which assures the reusability and reliability of this alloy. Although the time required for each test cycle in the *M-T* curve is about 2000 s, which is determined by the heating/cooling rate of 0.167 K/s of the PPMS, the magnetization
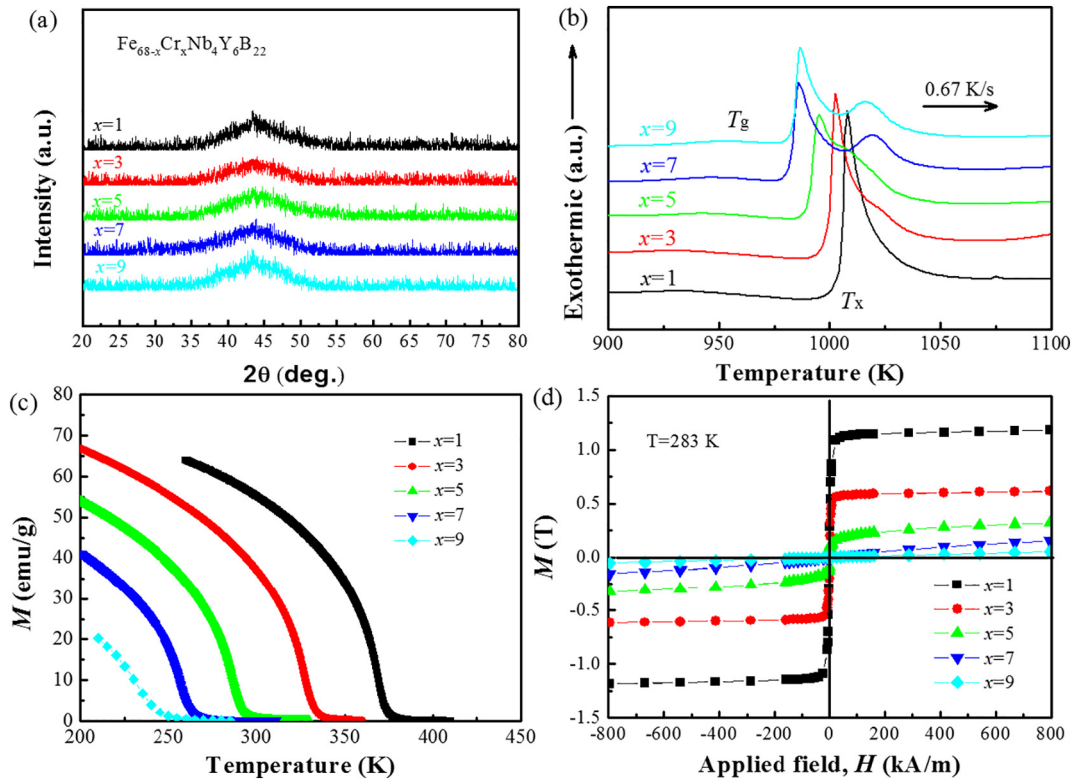
Fig. 1. (a) XRD patterns of the melt-spun $Fe_{68-x}Cr_xNb_4Y_6B_{22}$ (x = 1, 3, 5, 7, and 9 at%) amorphous ribbons. (b) DSC curves of the melt-spun amorphous ribbons. (c) Temperature dependence of the magnetization of the melt-spun $Fe_{68-x}Cr_xNb_4Y_6B_{22}$ (x = 1, 3, 5, 7, and 9 at%) amorphous ribbons under a low magnetic field of 0.01 T. (d) Magnetization curves of melt-spun amorphous ribbons at 283 K for fields up to 5 T.

transition of the actual magnetization response of this thermal-tuning amorphous alloy finishes within a much less time period. In order to further evaluate the magnetic response to temperature change, the dM/dT was derived for the $Fe_{63}Cr_5Nb_4Y_6B_{22}$ amorphous alloys through the cycles, as shown in Fig. 2(b). Two states (ferromagnetic and paramagnetic) of the alloy can be clearly distinguished, with the maximum |dM/dT| appearing around 300 K. With these cyclic measurements, it is proved that the magnetic properties of this material are very sensitive to the variation of thermal conditions. When the temperature is lower than 300 K, the $Fe_{63}Cr_5Nb_4Y_6B_{22}$ amorphous ribbon is ferromagnetic; when the temperature is higher than 300 K, the ribbon is paramagnetic.

3.1.4. Design of a thermal-tuning device

To verify the adaptability of the thermal-tuning amorphous alloy in wastewater treatment, a test device was designed using a permanent
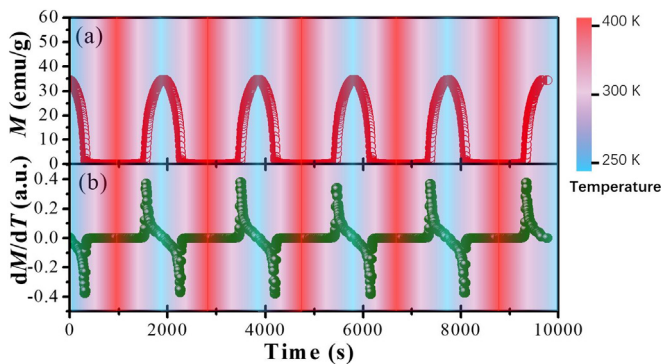

Fig. 2. (a) M-T curves and (b) dM/dT vs. time curves during the magnetically actuated thermal switch operational ON and OFF modes by heating and cooling for 5 cycles.

magnet, a $Fe_{63}Cr_5Nb_4Y_6B_{22}$ amorphous ribbon and a water tank in simulation of the working environment for dye degradation. The thermal-magnetic functionality of the alloy was demonstrated by the heating and cooling cycles, as shown in Fig. 3(a) and (b) (Videos 1 and 2 are provided in supplemental materials). When an external dye wastewater is filled in the tank at high temperature (343 K), the FAAs are paramagnetic and disperse into water to participate in the chemical reactions in the solution. When the wastewater is degraded and the temperature decreases, the FAAs are ferromagnetic and easily separated from the solution due to the strong magnetic force between the magnet and the amorphous ribbons. Then the degraded water can be released.

3.2. Degradation performance of $Fe_{63}Cr_5Nb_4Y_6B_{22}$ amorphous ribbons

3.2.1. Degradation performance at different temperatures

Fenton-like reactions were carried out using $Fe_{63}Cr_5Nb_4Y_6B_{22}$ amorphous ribbons to verify their applicability for dye degradation. According to previous research carried out by Wang et al. [43], FAAs have the best performance in decomposing rhodamine B at pH = 3, as Fenton-like reaction favors acidic solutions. So the MB degrading efficiency of the Fenton-like reactions using $Fe_{63}Cr_5Nb_4Y_6B_{22}$ amorphous ribbons was measured at pH = 3. Our reaction conditions were set as following: T = 283, 303, 323 and 343 K, initial H_2O_2 concentration (C_{H2O2}) = 2 mM, ribbon dosage = 0.5 g L^{-1}, initial MB concentration (C_{MB}) = 100 mg L^{-1}. As an example, typical decolorization phenomenon is observed during the Fenton-like reactions using $Fe_{63}Cr_5Nb_4Y_6B_{22}$ amorphous ribbons at 283 and 343 K as shown in Fig. 3(c) and (d), respectively. No color change of the MB solution with $Fe_{63}Cr_5Nb_4Y_6B_{22}$ ribbons at low temperature (283 K) was observed even after 56 min, while the hot MB solution (343 K) with the same reaction condition turns clear within 11 min.

To investigate the effect of temperature on the degradation process in detail, Fenton-like reactions using $Fe_{63}Cr_5Nb_4Y_6B_{22}$
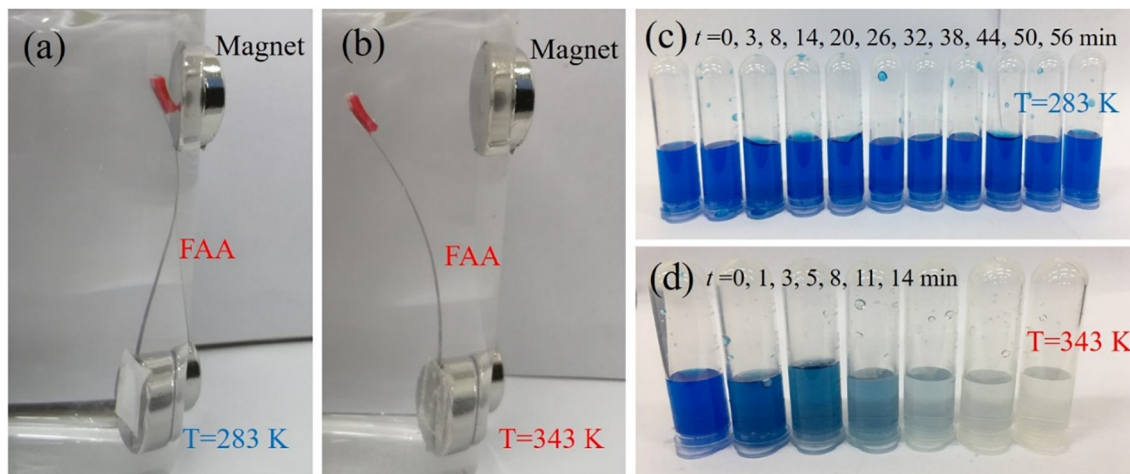
Fig. 3. Images of the magnetically actuated thermal switch models and corresponding experimental results for applied magnetic fields in the cooling and heating water at (a) 283 K and (b) 343 K. Visible color change of MB solutions during Fenton-like reactions using $Fe_{63}Cr_5Nb_4Y_6B_{22}$ amorphous ribbons at (c) 283 K and (d) 343 K.

amorphous ribbons were carried out at 283, 303, 323 and 343 K, respectively. UV–Vis absorbance spectra of the filtered MB solutions during these degradation experiments are shown in Fig. 4. Four adsorption peaks are observed for MB solutions at 247, 291, 618 and 653 nm. The peaks at 247 and 291 nm are from thiazine groups, while the other two peaks at 618 and 653 nm represent auxochrome and chromophore groups, respectively [44]. All of the four peaks decrease slowly at 283 and 303 K, but rapidly at 323 and 343 K,

corresponding to the concentration change of MB solution and the visualized decolorization phenomenon in Fig. 3(c) and (d). The XPS spectra in Fig. S2 confirmed that both the metallic and oxidized states of all the elements, including Fe, Cr, B, Y and Nb, appeared on the surface of melt-spun $Fe_{63}Cr_5Nb_4Y_6B_{22}$ ribbons, while only oxidized state of these elements was detected on the ribbons after degradation (323 K) [31,45,46]. This result confirms that chemical the decolorization involves chemical reactions, not just adsorption. As
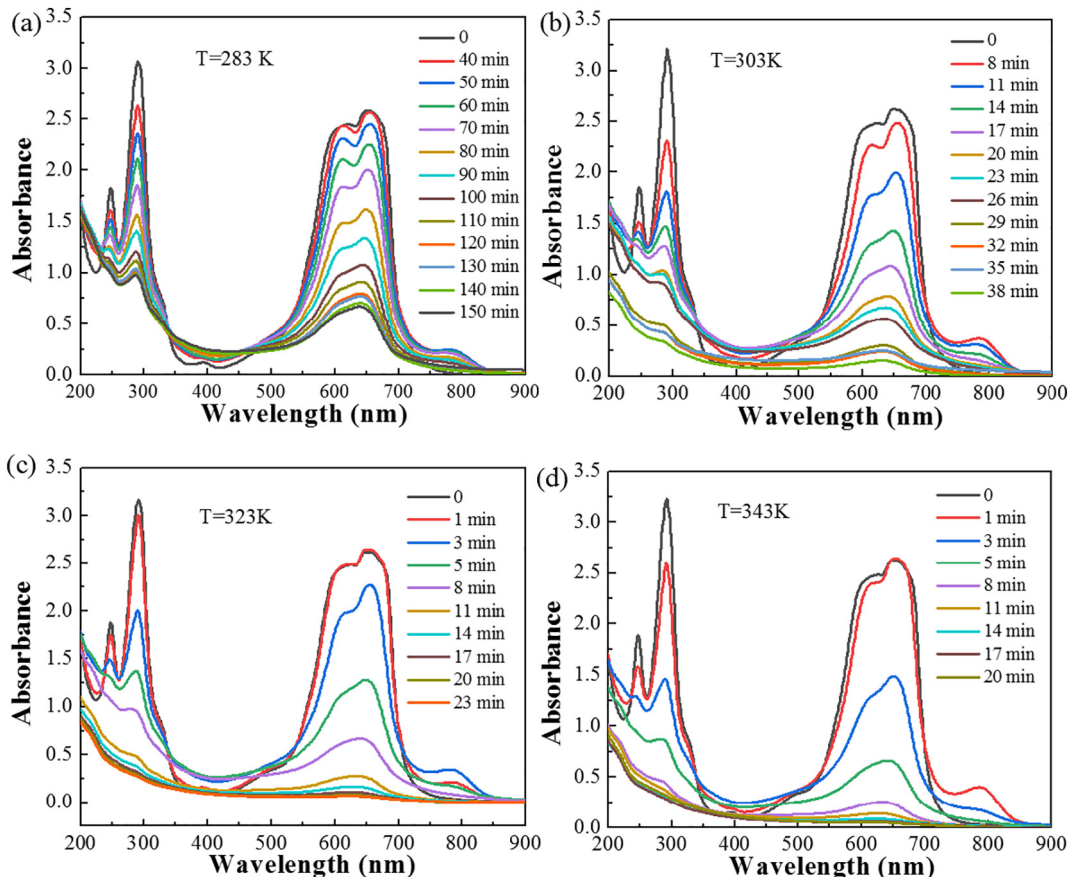
Fig. 4. UV absorption spectra during the Fenton-like reaction process using $Fe_{63}Cr_5Nb_4Y_6B_{22}$ amorphous ribbons at (a) 283 K, (b) 303 K, (c) 323 Kand (d) 343 K, respectively.

shown in Fig. S3, no characteristic absorption peaks appeared on the FTIR spectrum of melt-spun $Fe_{63}Cr_5Nb_4Y_6B_{22}$ ribbons, while several notable absorption from different organic functional groups showed on the FTIR spectrum of $Fe_{63}Cr_5Nb_4Y_6B_{22}$ ribbons after degradation (323 K) [47–50]. All the functional groups detected on the ribbon after degradation come from methylene blue solution or reaction products, thus the absorption of methylene blue on the ribbon, as well as the occurrence of Fenton-like reaction can be further confirmed. Raman spectra of the melt-spun and after-degradation (323 K) $Fe_{63}Cr_5Nb_4Y_6B_{22}$ ribbons were recorded as shown in Fig. S3. For melt-spun ribbon, the tiny peaks from Fe_2O_3 (237 and 602 cm^{-1}), CrO_3 (269 and 326 cm^{-1}) and Fe_3O_4 (627 cm^{-1}) were detected [51,52], showing that a small amount iron and chromium were oxidized on the melt-spun ribbons. For the ribbons after degradation, other than the small peaks detected on melt-spun ribbons, a broad and large peak ranging from 987 to 1700 cm^{-1} are attributed to FeOOH, Fe_2O_3 and organic compounds [51,53,54], proving a large amount of zero-valent iron was fully oxidized to ferric iron and the organic molecules were adsorbed on the surface of ribbons. The Raman results further confirm the Fenton-reaction involve chemical processes, not just physical adsorption.

The normalized concentration of the MB solution during the degradation process at different temperatures was obtained with the peak values at 653 nm, as shown in Fig. 5. The concentration of the solutions reacting at different temperatures remains almost unchanged during the first 3 min, which is believed to be the time required for the generation of •OH groups and the •OH groups approaching the dye molecules. According to the data derived from UV–Vis absorbance spectra, no concentration change is observed for the reaction at 283 K within 30 min, which is consistent with the direct visual observation in Fig. 3(c). There is still 12% MB left in the solution after 30 min for the degradation experiment at 303 K. In contrast, in hot water, including 323 and 343 K, it requires 17 and 11 min to reduce C_t/C_0 to <5%, respectively. $C_t/C_0 < 5\%$ (when 95% of MB is decomposed) is set as the degradation completion target for instrumental fluctuation in this work. The positive influence of temperature on the degradation process is verified by the decreased reaction time with the increased solution temperature. The generation rate of the •OH group during the Fenton reaction process is accelerated by the raised temperature, thus the decolorization efficiency is enhanced. The high catalytic efficiency of $Fe_{63}Cr_5Nb_4Y_6B_{22}$ amorphous ribbons at high temperatures fits very well with the design principles of the thermal-tuning wastewater remediation system.

After the first 3 min of the reaction, the degradation kinetics can be described by the pseudo-first-order equation as given below:

$$C_t = C_0 * \exp(-kt) \tag{1}$$

where k is the reaction rate constant (min^{-1}), C_t is the concentration of MB ($mg\,L^{-1}$) at time t, C_0 is the initial concentration of MB ($mg\,L^{-1}$) and

t is the reaction time (min). Then the degradation reaction rate constant can be derived as follow:

$$k = \ln\left(\frac{C_0}{C_t}\right)/t \tag{2}$$

According to the $\ln(C_0/C_t)$ vs. t curves plotted in Fig. 5(b), the reaction rate constants of amorphous ribbons in the Fenton-like reactions are 0, 0.088, 0.182, and 0.239 min^{-1} at 283, 303, 323 and 343 K, respectively. Dramatic improvement of the reaction rate with increased solution temperature was observed.

As the reaction rate is highly affected by temperature, the thermal activation energy for the degradation of MB with amorphous ribbons was derived using the Arrhenius-type equation, as shown below:

$$\ln k = -\frac{\Delta E}{RT} + \ln A \tag{3}$$

where k is the reaction rate constant at different temperatures, ΔE is the reaction activation energy, R is the gas constant and A is a constant. The $\ln k$ vs. $-1/RT$ plots were generated to get ΔE, as shown in Fig. 5(c). The reaction activation energy of amorphous ribbon is 21.8 kJ mol/1. The lower activation energy of $Fe_{63}Cr_5Nb_4Y_6B_{22}$ amorphous ribbons contributes to their better performance at high temperature in the Fenton-like reaction. The thermal activation energy barrier of the $Fe_{63}Cr_5Nb_4Y_6B_{22}$ in the present study is lower than that previously found for Fe-based amorphous alloys, as summarized in Table 1. The low thermal activation energy barrier may come from the decreased thermal stability of the alloys with Cr addition as discussed above. With lower thermal stability, the increased solution temperature lead to a sharper decrease of the atomic interactions in the alloy and reduce the required energy to break of the bonding between iron and other elements. As shown in Table 1, only $Fe_{63}Cr_5Nb_4Y_6B_{22}$ amorphous ribbon synthesized in this work present low activation energy barrier and room-temperature T_C simultaneously, which makes the alloy more suitable as a thermal-tuning material for dye removal.

3.2.2. Corrosion resistance

The catalytic performance of FAAs at different temperatures in the Fenton-like reaction is usually related to their corrosion resistance, as the oxidized layer may impede the electron transfer from Fe^0 to the solution [44]. To evaluate the effect of temperature on the corrosion behavior of $Fe_{63}Cr_5Nb_4Y_6B_{22}$ amorphous alloys, the potentiodynamic polarization measurement of the ribbons in the MB solution at 283 and 343 K was performed (C_{H2O2} = 1 mM, C_{MB} = 100 mg L^{-1}). Fig. 6 shows the polarization curves of the as-quenched $Fe_{63}Cr_5Nb_4Y_6B_{22}$ ribbons measured at different temperatures. When the solution is 283 K, the $Fe_{63}Cr_5Nb_4Y_6B_{22}$ amorphous alloys passivated with wide passive regions exceeding 0.55 V, low passive current density
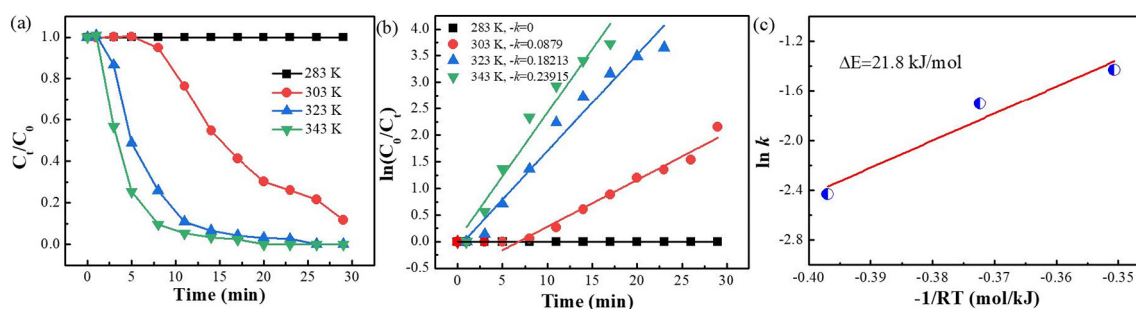
Fig. 5. (a) Normalized concentration change of MB solutions during the Fenton-like reactions using $Fe_{63}Cr_5Nb_4Y_6B_{22}$ amorphous ribbons at different temperatures; (b) the $\ln(C_t/C_0)$ vs. time curves for $Fe_{63}Cr_5Nb_4Y_6B_{22}$ amorphous ribbons at different temperatures; (d) $\ln k$ vs. $-1/RT$ curves for $Fe_{63}Cr_5Nb_4Y_6B_{22}$ amorphous ribbons (pH = 3, C_{H2O2} = 1 mM, ribbon dosage = 0.5 g L^{-1}, C_{MB} = 100 mg L^{-1}).

Table 1
Comparable results of Curie temperature of various Fe-based amorphous alloys and the reaction activation energy for dye degradation using these alloys.

Compositions	T_C (K)	Dosage (g L^{-1})	Dye	ΔE (kJ/mol)	Ref.
$(Fe_{71.2}B_{24}Y_{4.8})_{96}Nb_4$	470	0.2	Methyl orange	22.6	[32,55]
$Fe_{80}P_{13}C_7$	579	0.5	Methyl blue	22.8	[31,58]
$Fe_{78}Si_9B_{13}$	708	0.5	Methyl blue	34.8	[31,59]
$(Fe_{0.99}Mo_{0.01})_{78}Si_9B_{13}$	665	0.2	Direct blue 2B	28.4	[27,60]
$Fe_{84}B_{16}$	590	0.2	Direct blue 6	25.43	[61,62]
$Fe_{73}Nb_3Si_7B_{17}$	560	0.5	Bule azo Dye	78	[20,63]
$Fe_{63}Cr_5Nb_4Y_6B_{22}$	300	0.5	Methyl blue	21.8	This work

3.24×10^{-6} A·cm^{-2}, and low transpassive potential 0.76 V at 283 K. The obvious passivation region in the polarization curve reveals that a uniform and complete passive film form on the surface of the alloy, resulting in the excellent corrosion resistance for $Fe_{63}Cr_5Nb_4Y_6B_{22}$ amorphous ribbons at low temperature. Abrupt changes of the polarization curves occurred when temperature increased from 283 to 343 K, indicating the dramatic changes of the overall corrosion performance. The alloy at high temperature suffers from corrosion by an anodic polarization without passive region. The corrosion potential of the ribbon at 343 K is −0.34 V, which is much lower than 0.11 V for that at 283 K. These results indicate that the corrosion resistance of the ribbons at 343 K is much worse than that at 283 K, which may explain the better degradation performance of the ribbons in hot MB solution.

3.2.3. Surface morphology and elemental information

As the degradation reactions occur on the surface of the ribbons, it is crucial to understand the structure change of the surface for the $Fe_{63}Cr_5Nb_4Y_6B_{22}$ amorphous ribbons during the Fenton-like reaction. Fig. 7 shows the surface morphologies and elemental composition of the as-quenched and reacted $Fe_{63}Cr_5Nb_4Y_6B_{22}$ ribbons, respectively. As seen from Fig. 7(a) and (b), the as-quenched $Fe_{63}Cr_5Nb_4Y_6B_{22}$ ribbon surface is practically smooth without any apparent defect. The peaks in the EDS are identified as Fe, Y, Nb, B and Cr elements. Fig. 7(c) and (d) show the surface morphology and the corresponding EDS result of the reacted $Fe_{63}Cr_5Nb_4Y_6B_{22}$ ribbon. The surface of the ribbon after Fenton-like reaction is severely corroded and porous-like, which is consistent with the result from the electrochemical analysis. The decreased atomic bonding with Cr addition may promote the escape of some atoms and the formation of the porous structures. It is found that the amount of O increases dramatically, indicating the formation of oxidized layer during the reaction. The amount of Fe reduce sharply after reaction as Fe is gradually consumed for the generation of •OH, which in turn causes an efficient degradation of the dye molecules. As the oxidation
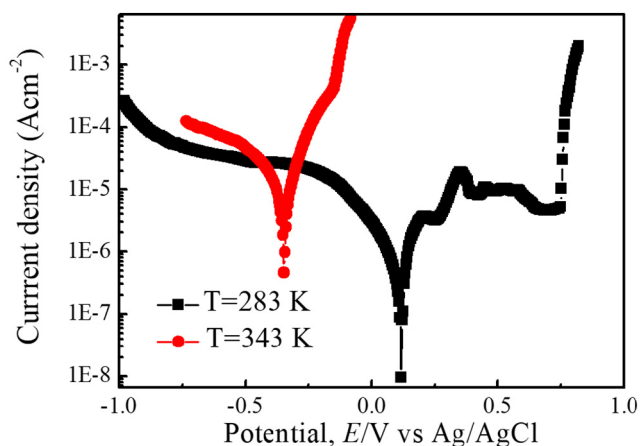
Fig. 6. Potentiodynamic polarization curves of $Fe_{63}Cr_5Nb_4Y_6B_{22}$ amorphous ribbons in MB solutions at 283 K and 343 K (pH = 3, C_{H2O2} = 1 mM, C_{MB} = 100 mg L^{-1}).

films, coming from a series of oxidation reactions of Fe and other elements, formed on the originally smooth ribbon surface are not densely packed, the mass and electron transfer channel is clear, leading to the high degradation efficiency.

3.2.4. Mechanism of the high degrading efficiency

It is interesting to note that even though the amorphous ribbons contain as much as 20 at.% metalloid elements, they are still efficient catalysis for degrading MB. It indicates that the metastable bonding between the atoms in Fe-based metallic glasses allows the Fe atoms to keep high reaction activity in the dye solution. For $Fe_{63}Cr_5Nb_4Y_6B_{22}$ metallic glass, it is quite reasonable to propose that inhomogeneous structures of Fe-rich clusters and Fe-poor regions appear in the alloy due to the existence of the Y atoms with large atomic radius [55]. The inhomogeneous amorphous structure may explain the relative high catalytic efficiency of the $Fe_{63}Cr_5Nb_4Y_6B_{22}$ amorphous ribbons for degrading MB. As is well known, a typical redox reaction is responsible for the degradation of azo dyes using Fenton-like reactions [56]. The ability of the reducing agent to lose electrons partly determines the degradation efficiency. Compared with the Fe-rich nano-clusters, the Fe-poor regions mainly coordinate with the metalloid elements and exhibit a relatively low electronegativity. Thus, it is easy to envision galvanic cells between them, which promote the Fe atoms in the Fe-rich clusters to lose electrons and take part in the degradation reaction. Generally, the local atomic Fe-rich and Fe-poor clusters are in nanometer scale and assumed to be homogeneously distributing in the amorphous alloys [34,38,57]. The large quantity of nano-galvanic cells is expected to have a strong affinity for donating electrons to the reaction [31,32]. Besides, the reduced atomic bonding strength of the alloy due to the introduction of Cr elements also contributes to the high reaction activity of iron, especially at high temperatures.

3.3. Adaptability of $Fe_{63}Cr_5Nb_4Y_6B_{22}$ amorphous ribbons

3.3.1. Effects of environmental variables

Other than solution temperature, the experimental parameters of Fenton-like reactions, including pH, initial H_2O_2 concentration (C_{H2O2}), MB concentration (C_{MB}) and ribbon dosage, also have great impact on the degradation performance of Fe-based amorphous ribbons. Effect of pH on the Fenton-like reaction using $Fe_{63}Cr_5Nb_4Y_6B_{22}$ amorphous ribbons was investigated by setting other reaction parameters as constants: T = 323 K, C_{H2O2} = 2 mM, C_{MB} = 100 mg L^{-1} and ribbon dosage = 0.5 g L^{-1}. As shown in Fig. 8(a), MB was completely degraded after 17 min when pH of the solution equals to 2 and 3, while no MB concentration change was observed within 60 min for solutions with pH = 5, 7 and 9. According to the result, $Fe_{63}Cr_5Nb_4Y_6B_{22}$ amorphous ribbons have good MB degrading ability only in strong acidic solutions. However, the degrading performance of the ribbons didn't increase with pH decreasing from 3 to 2, which resulted from the promotion of hydrogen evolution reaction at pH = 2 [31].

Experiments with different initial H_2O_2 concentration were carried out to investigate effect of H_2O_2 on the Fenton-like reactions as shown in Fig. 8(b), with other experimental parameters set as: T = 323 K, pH = 3, C_{MB} = 100 mg L^{-1} and ribbon dosage = 0.5 g L^{-1}. Without H_2O_2, no decrease of MB concentration was detected within 60 min. Although Fe^0 can decompose organic molecules through oxidation-reduction reactions, the reaction rate is much slower than Fenton-like reactions. With 0.5 mM H_2O_2 addition, the MB concentration decreases sharply in the first 11 min, then reaches a platform for the rest of time. The normalized concentration change (C_t/C_0) of MB after 60 min was 35%. This result reveals that a critical amount of H_2O_2 is required for Fenton-like reactions. After the complete consumption of H_2O_2, the reaction changed from the rapid Fenton-like degradation to the slow oxidation-reduction type, thus MB concentration stayed almost unchanged afterwards. With the initial H_2O_2 concentration increasing to 2 and 5 mM, the
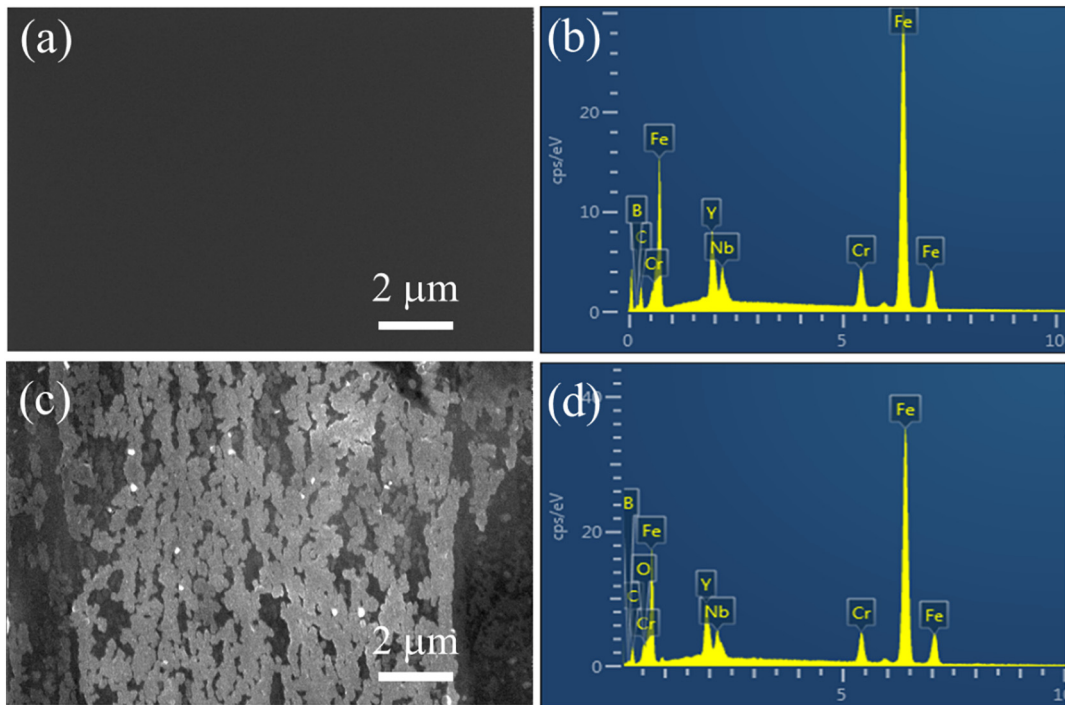
Fig. 7. (a) SEM micrographs of as-quenched $Fe_{63}Cr_5Nb_4Y_6B_{22}$ ribbon, (b) EDS analysis of the as-quenched ribbon, (c) SEM micrographs of the reacted $Fe_{63}Cr_5Nb_4Y_6B_{22}$ ribbon, (d) EDS analysis of the reacted ribbons.

decomposition finished within 17 and 8 min, respectively. The higher concentration of H_2O_2 in solution results in the faster generation of the oxidative •OH radicals, leading to the acceleration of reaction. However, the Fenton-like reaction was slowed down to 11, 11 and 25 min with further increasing H_2O_2 concentration to 10, 30 and 50 mM, as excessive H_2O_2 can react with the generated ·OH to produce HO_2• radicals. Thus, the optimum concentration of H_2O_2 is 5 mM for current reaction settings.
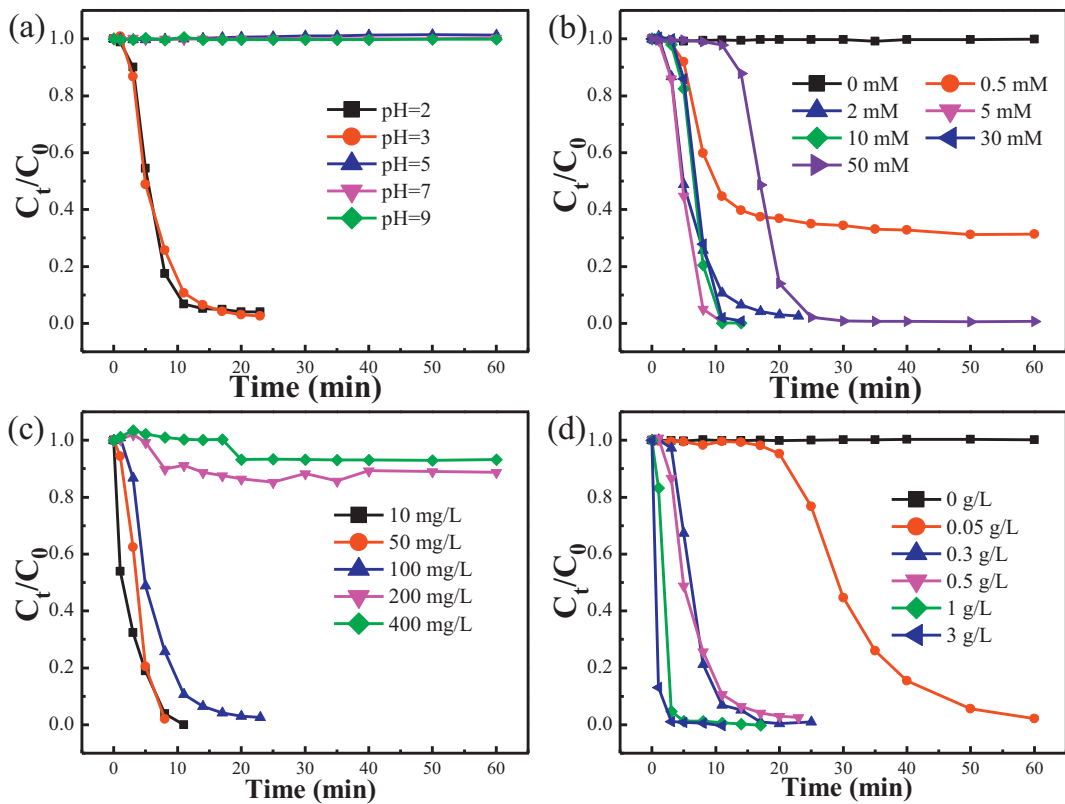
Fig. 8. Effects of (a) pH, (b) initial H_2O_2 concentration, (c) MB concentration, and (d) ribbon dosage on the normalized concentration of MB solutions during Fenton-like reactions using $Fe_{63}Cr_5Nb_4Y_6B_{22}$ amorphous ribbons.
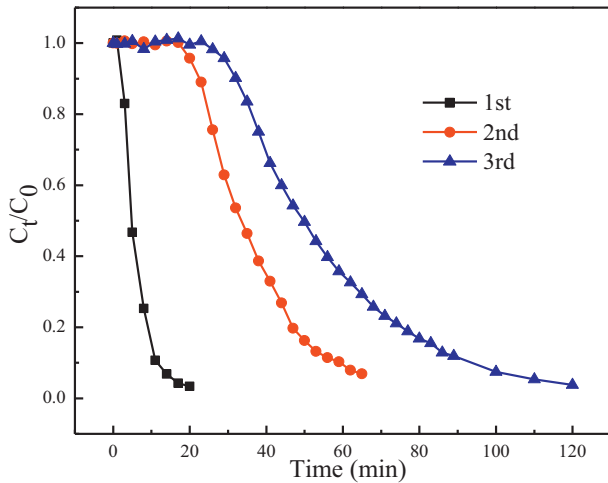
Fig. 9. Normalized concentration change of MB solutions during Fenton-like reactions using $Fe_{63}Cr_5Nb_4Y_6B_{22}$ amorphous ribbons from 1st to 3rd degradation cycles ($T = 323$ K, pH = 3, $C_{H2O2} = 2$ mM, $C_{MB} = 100$ mg L^{-1} and ribbon dosage = 0.5 g L^{-1}).

Effect of MB concentration on the Fenton-like experiments using $Fe_{63}Cr_5Nb_4Y_6B_{22}$ amorphous ribbons were investigated with other reaction parameters set as: $T = 323$ K, pH = 3, $C_{H2O2} = 2$ mM and ribbon dosage = 0.5 g L^{-1}. As expected, the reaction time required for degradation increased with increasing MB concentration [Fig. 8(c)]. When the solution was dilute, eg. 10 and 50 mg L^{-1}, decolorization processes finished within 8 min. When MB solution was concentrated (>200 mg L^{-1}), only a small amount of MB (about 10%) was decomposed at the beginning of the reaction process, and then no further decrease of MB concentration was observed within 60 min. Wastewater with MB concentration >200 mg L^{-1} is beyond the degrading ability of the current experimental settings.

Materials cost can be reduced with optimized ribbon dosage. Reaction process with different ribbon dosage was carried out with other experimental parameters set as: $T = 323$ K, pH = 3, $C_{H2O2} = 2$ mM and $C_{MB} = 100$ mg L^{-1}. As shown in Fig. 8(d), no decolorization was observed within 60 min without adding ribbons in MB solution, indicating that the influence of decolorization caused by H_2O_2 itself can be ignored in this work. When ribbon dosage = 0.05, 0.3, 0.5, 1 and 3 g L^{-1}, the time required for complete MB degradation were 50, 17, 17, 5 and 3 min, respectively. The decomposition time decreased almost linearly with increased dosage of $Fe_{63}Cr_5Nb_4Y_6B_{22}$ amorphous ribbon, which is reasonable as more reaction sites are available with larger surface area.

3.3.2. Stability and reusability

Stability of the designed system depends on the reusability of $Fe_{63}Cr_5Nb_4Y_6B_{22}$ amorphous ribbons. Cyclic tests of the Fenton-like reactions using $Fe_{63}Cr_5Nb_4Y_6B_{22}$ amorphous ribbons were carried out at 323 K to investigate the reusability of the ribbons. As shown in Fig. 9, the degradation time increased from 17 min to 65 and 120 min from the first cycle to the second and third cycles. The reduced amount of Fe^0 and the formed passive films on the surface of ribbons during reaction prolonged the decolorization time in the second and third cycles. Subsequent work will be carried out to improve the reusability of the current system.

3.4. Illustration of the working principle

Based on the above analyses, the illustration of the thermally-controlled cycles of MB degradation process using $Fe_{63}Cr_5Nb_4Y_6B_{22}$ amorphous alloys can be drawn in Fig. 10. As the $Fe_{63}Cr_5Nb_4Y_6B_{22}$ ribbon is in a nonequilibrium state due to the amorphous structure, it is thermodynamically less stable and has higher reaction activity than its crystalline counterparts. Besides, the heterogeneous nature of the $Fe_{63}Cr_5Nb_4Y_6B_{22}$ amorphous materials accelerates the electron transportation for the Fenton-like reaction. As a result, the surface-activated degrading reactions occur more rapidly with the amorphous ribbons. Changing the temperature of the solution induces the reversible ferromagnetic to paramagnetic transition. In the newly filled wastewater, usually with a temperature higher than 303 K, the amorphous ribbons are paramagnetic and automatically disperse in wastewater. Even under magnetic stirring, the ribbons don't aggregate and their surface can expose to the dye molecules and other pollutants in wastewater. After the iron-activation of peroxides, these dye molecules are oxidized by the produced radical species (•OH) near the ribbon surface. At the same time, the dissociative dye molecules are decomposed by free radicals in the solution. When the temperature of the wastewater is reduced to <303 K, the amorphous ribbons are ferromagnetic and easy to be recycled in the magnetic fields. After the ribbons are magnetically attracted to the magnet, remediated water can be released. It is worthy to note that, as the high-temperature dye wastewater usually cool down in the air during the degradation process, there is no need to change the environment artificially, which saves a considerable amount of energy for industrial applications.

4. Conclusions

In this work, a novel thermal-tuning $Fe_{63}Cr_5Nb_4Y_6B_{22}$ amorphous alloy for automatically recycled dye degradation was designed by
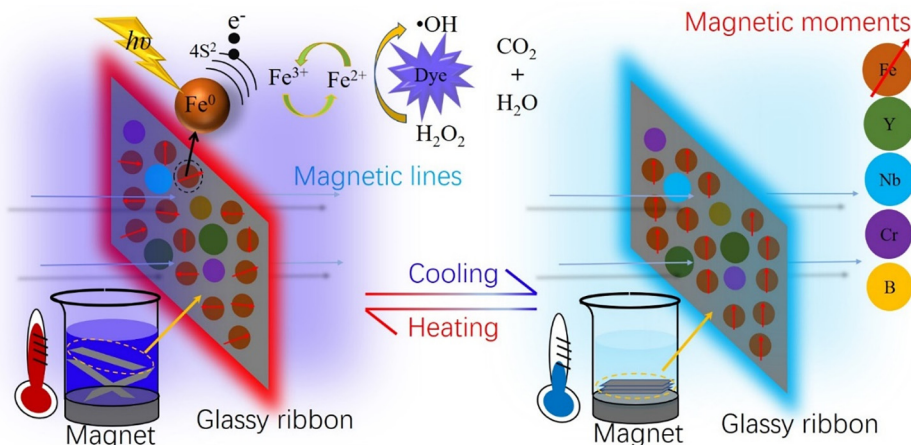
Fig. 10. Illustration of reversible thermal-tuning $Fe_{63}Cr_5Nb_4Y_6B_{22}$ amorphous alloys for MB degradation during heating and cooling processes.

comprehensively utilizing the soft-magnetic and catalytic properties of the alloy. When an external dye wastewater is applied (high temperature), the FAAs become paramagnetic and disperse into the solution to participate in degradation process. When the wastewater has been degraded and the temperature is reduced, the FAAs change to ferromagnetic and can be collected magnetically by the permanent magnet, which makes the discharge of the wastewater easy. It is proposed that the large amount of nano-sized Fe-rich clusters and Fe-poor regions may provide numerous nanogalvanic cells to accelerate the electron transportation from iron to the solution and therefore, decompose organic chemicals efficiently. The thermal activation energy barrier for the degradation reaction is as low as 21.8 kJ/mol. These findings not only provide a new highly-efficient and low cost commercial method for dye wastewater treatments, but also find a way to use the excellent magnetic and chemical properties of FAAs simultaneously.

Author contributions

Acknowledgements

References

[1] C.F. Zhang, L.G. Qiu, F. Ke, Y.J. Zhu, Y.P. Yuan, G.S. Xu, X. Jiang, A novel magnetic recyclable photocatalyst based on a core-shell metal-organic framework Fe_3O_4@MIL-100(Fe) for the decolorization of methylene blue dye, J. Mater. Chem. A 1 (2013) 14329–14334.

[2] M.M. Khan, S.A. Ansari, D. Pradhan, M.O. Ansari, D.H. Han, J. Lee, M.H. Cho, Band gap engineered TiO_2 nanoparticles for visible light induced photoelectrochemical and photocatalytic studies, J. Mater. Chem. A 2 (2014) 637–644.

[3] W.G. Kuo, Decolorizing dye waste-water with Fenton reagent, Water Res. 26 (1992) 881–886.

[4] P.C. Vandevivere, R. Bianchi, W. Verstraete, Treatment and reuse of wastewater from the textile wet-processing industry: review of emerging technologies, J. Chem. Technol. Biotechnol. 72 (1998) 289–302.

[5] S.X. Liang, Z. Jia, W.C. Zhang, X.F. Li, W.M. Wang, H.C. Lin, L.C. Zhang, Ultrafast activation efficiency of three peroxides by $Fe_{78}Si_9B_{13}$ metallic glass under photo-enhanced catalytic oxidation: a comparative study, Appl. Catal. B Environ. 221 (2018) 108–118.

[6] I.K. Konstantinou, T.A. Albanis, TiO_2-assisted photocatalytic degradation of azo dyes in aqueous solution: kinetic and mechanistic investigations - a review, Appl. Catal. B Environ. 49 (2004) 1–14.

[7] R. Sharma, P. Thakur, P. Kumar, N. Sharma, V. Sharma, Nanomaterials for high frequency device and photocatalytic applications: Mg-Zn-Ni ferrites, J. Alloys Compd. 746 (2018) 532–539.

[8] M. Ghanbari, M. Sabet, M. Salavati-Niasari, Synthesis of different morphologies of Cu2CdI4/CuI nanocomposite via simple hydrothermal method, J. Mater. Sci. Mater. Electron. 27 (2016) 11092–11101.

[9] M. Ghanbari, F. Ansari, M. Salavati-Niasari, Simple synthesis-controlled fabrication of thallium cadmium iodide nanostructures via a novel route and photocatalytic investigation in degradation of toxic dyes, Inorg. Chim. Acta 455 (2017) 88–97.

[10] C.C. Jiang, S.Y. Pang, F. Ouyang, J. Ma, J. Jiang, A new insight into Fenton and Fenton-like processes for water treatment, J. Hazard. Mater. 174 (2010) 813–817.

[11] L.J. Sun, Y.Y. Yao, L. Wang, Y.J. Mao, Z.F. Huang, D.C. Yao, W.Y. Lu, W.X. Chen, Efficient removal of dyes using activated carbon fibers coupled with 8-hydroxyquinoline ferric as a reusable Fenton-like catalyst, Chem. Eng. J. 240 (2014) 413–419.

[12] S. Rodriguez, L. Vasquez, D. Costa, A. Romero, A. Santos, Oxidation of Orange G by persulfate activated by Fe(II), Fe(III) and zero valent iron (ZVI), Chemosphere 101 (2014) 86–92.

[13] H. Katsumata, S. Kaneco, T. Suzuki, K. Ohta, Y. Yobiko, Degradation of linuron in aqueous solution by the photo-Fenton reaction, Chem. Eng. J. 108 (2005) 269–276.

[14] M.I. Pariente, F. Martinez, J.A. Melero, J.A. Botas, T. Velegraki, N.P. Xekoukoulotakis, D. Mantzavinos, Heterogeneous photo-Fenton oxidation of benzoic acid in water: effect of operating conditions, reaction by-products and coupling with biological treatment, Appl. Catal. B Environ. 85 (2008) 24–32.

[15] L.W. Matzek, K.E. Carter, Activated persulfate for organic chemical degradation: a review, Chemosphere 151 (2016) 178–188.

[16] Y.F. Zhao, J.J. Si, J.G. Song, Q. Yang, X.D. Hui, Synthesis of Mg-Zn-Ca metallic glasses by gas-atomization and their excellent capability in degrading azo dyes, Mater. Sci. Eng., B 181 (2014) 46–55.

[17] P.P. Wang, J.Q. Wang, H. Li, H. Yang, J.T. Huo, J.G. Wang, C.T. Chang, X.M. Wang, R.W. Li, G. Wang, Fast decolorization of azo dyes in both alkaline and acidic solutions by Al-based metallic glasses, J. Alloys Compd. 701 (2017) 759–767.

[18] X.D. Qin, Z.W. Zhu, G. Liu, H.M. Fu, H.W. Zhang, A.M. Wang, H. Li, H.F. Zhang, Ultra-fast degradation of azo dyes catalyzed by cobalt-based metallic glass, Sci. Rep. 5 (2015) 18226.

[19] C.Q. Zhang, Q.L. Sun, K.G. Liu, From adsorption to reductive degradation: different decolorization properties of metallic glasses based on different iron-group elements, J. Alloys Compd. 741 (2018) 1040–1047.

[20] J.Q. Wang, Y.H. Liu, M.W. Chen, G.Q. Xie, D.V. Louzguine-Luzgin, A. Inoue, J.H. Perepezko, Rapid degradation of Azo dye by Fe-based metallic glass powder, Adv. Funct. Mater. 22 (2012) 2567–2570.

[21] C. Suryanarayana, A. Inoue, Iron-based bulk metallic glasses, Int. Mater. Rev. 58 (2013) 131–166.

[22] Z.P. Lu, C.T. Liu, J.R. Thompson, W.D. Porter, Structural amorphous steels, Phys. Rev. Lett. 92 (2004) 245503.

[23] Y. Tang, Y. Shao, N. Chen, X. Liu, S.Q. Chen, K.F. Yao, Insight into the high reactivity of commercial Fe-Si-B amorphous zero-valent iron in degrading azo dye solutions, RSC Adv. 5 (2015) 34032–34039.

[24] R. Li, X.J. Liu, H. Wang, Y. Wu, K.C. Chan, Z.P. Lu, Flexible glassy grid structure for rapid degradation of azo dye, Mater. Des. 155 (2018) 346–351.

[25] Z. Jia, W.C. Zhang, W.M. Wang, D. Habibi, L.C. Zhang, Amorphous $Fe_{78}Si_9B_{13}$ alloy: an efficient and reusable photo-enhanced Fenton-like catalyst in degradation of cibacron brilliant red 3B-A dye under UV-vis light, Appl. Catal. B Environ. 192 (2016) 46–56.

[26] Z. Jia, X.G. Duan, P. Qin, W.C. Zhang, W.M. Wang, C. Yang, H.Q. Sun, S.B. Wang, L.C. Zhang, Disordered atomic packing structure of metallic glass: toward ultrafast hydroxyl radicals production rate and strong electron transfer ability in catalytic performance, Adv. Funct. Mater. 27 (2017), 1702258.

[27] C.Q. Zhang, Z.W. Zhu, H.F. Zhang, Z.Q. Hu, On the decolorization property of Fe-Mo-Si-B alloys with different structures, J. Non-Cryst. Solids 358 (2012) 61–64.

[28] C.C. Yang, X.F. Bian, J.F. Yang, Enhancing the efficiency of wastewater treatment by addition of Fe-based amorphous alloy powders with H2O2 in ferrofluid, Funct. Mater. Lett. 7 (2014) 1450028.

[29] S.X. Liang, Z. Jia, W.C. Zhang, W.M. Wang, L.C. Zhang, Rapid malachite green degradation using $Fe_{73.5}Si_{13.5}B_9Cu_1Nb_3$ metallic glass for activation of persulfate under UV–Vis light, Mater. Des. 119 (2017) 244–253.

[30] J.C. Wang, Z. Jia, S.X. Liang, P. Qin, W.C. Zhang, W.M. Wang, T.B. Sercombe, L.C. Zhang, $Fe_{73.5}Si_{13.5}B_9Cu_1Nb_3$ metallic glass: rapid activation of peroxymonosulfate towards ultrafast Eosin Y degradation, Mater. Des. 140 (2018) 73–84.

[31] Q.Q. Wang, M.X. Chen, P.H. Lin, Z.Q. Cui, C.L. Chu, B.L. Shen, Investigation of FePC amorphous alloys with self-renewing behaviour for highly efficient decolorization of methylene blue, J. Mater. Chem. A 6 (2018) 10686.

[32] S.H. Xie, P. Huang, J.J. Kruzic, X.R. Zeng, H.X. Qian, A highly efficient degradation mechanism of methyl orange using Fe-based metallic glass powders, Sci. Rep. 6 (2016) 21947.

[33] Z. Jia, X.G. Duan, W.C. Zhang, W.M. Wang, H.Q. Sun, S.B. Wang, L.C. Zhang, Ultra-sustainable $Fe_{78}Si_9B_{13}$ metallic glass as a catalyst for activation of persulfate on methylene blue degradation under UV-Vis light, Sci. Rep. 6 (2016), 38520.

[34] W.M. Yang, H.S. Liu, Y.C. Zhao, A. Inoue, K.M. Jiang, J.T. Huo, H.B. Ling, Q. Li, B.L. Shen, Mechanical properties and structural features of novel Fe-based bulk metallic glasses with unprecedented plasticity, Sci. Rep. 4 (2014) 6233.

[35] P. Alvarez-Alonso, J.D. Santos, M.J. Perez, C.F. Sanchez-Valdes, J.L.S. Llamazares, P. Gorria, The substitution effect of chromium on the magnetic properties of $(Fe_{1−x}Cr_x)_{80}Si_6B_{14}$ metallic glasses ($0.02 \le x \le 0.14$), J. Magn. Magn. Mater. 347 (2013) 75–78.

[36] R. Yapp, B.E. Watts, F. Leccabue, Characterisation of amorphous Fe-Cr-Si-B alloys, J. Magn. Magn. Mater. 215 (2000) 300–302.

[37] D.D. Xu, B.L. Zhou, Q.Q. Wang, J. Zhou, W.M. Yang, C.C. Yuan, L. Xue, X.D. Fan, L.Q. Ma, B.L. Shen, Effects of Cr addition on thermal stability, soft magnetic properties and corrosion resistance of FeSiB amorphous alloys, Corros. Sci. 138 (2018) 20–27.

[38] Q. Yu, X.D. Wang, H.B. Lou, Q.P. Cao, J.Z. Jiang, Atomic packing in Fe-based metallic glasses, Acta Mater. 102 (2016) 116–124.

[39] A. Afkhami, M. Saber-Tehrani, H. Bagheri, Modified maghemite nanoparticles as an efficient adsorbent for removing some cationic dyes from aqueous solution, Desalination 263 (2010) 240–248.

[40] J.G. Speight, Lang's Handbook of Chemistry, 16th ed. McGraw-Hill Professional, 2005.

[41] A. Takeuchi, A. Inoue, Classification of bulk metallic glasses by atomic size difference, heat of mixing and period of constituent elements and its application to characterization of the main alloying element, Mater. Trans. 46 (2005) 2817–2829.

[42] C.L. Chien, Mossbauer study of an amorphous magnetic solid containing Cr, Phys. Rev. B 19 (1979) 81–86.

[43] X.F. Wang, Y. Pan, Z.R. Zhu, J.L. Wu, Efficient degradation of rhodamine B using Fe-based metallic glass catalyst by Fenton-like process, Chemosphere 117 (2014) 638–643.

[44] Z. Jia, J. Kang, W.C. Zhang, W.M. Wang, C. Yang, H. Sun, D. Habibi, L.C. Zhang, Surface aging behaviour of Fe-based amorphous alloys as catalysts during heterogeneous photo Fenton-like process for water treatment, Appl. Catal. B Environ. 204 (2017) 537–547.

[45] J.J. Si, X.H. Chen, Y.H. Cai, Y.D. Wu, T. Wang, X.H. Hui, Corrosion behavior of Cr-based bulk metallic glasses in hydrochloric acid solutions, Corros. Sci. 107 (2016) 123–132.

[46] H.B. Fan, W. Zheng, G.Y. Wang, P.K. Liaw, J. Shen, Corrosion behavior of $Fe_{41}Co_7Cr_{15}Mo_{14}C_{15}B_6Y_2$ bulk metallic glass in sulfuric acid solutions, Metall. Mater. Trans. A 42a (2011) 1524–1533.

[47] T.H. Liu, Y.H. Li, Q.J. Du, J.K. Sun, Y.Q. Jiao, G.M. Yang, Z.H. Wang, Y.Z. Xia, W. Zhang, K.L. Wang, H.W. Zhu, D.H. Wu, Adsorption of methylene blue from aqueous solution by graphene, Colloids Surf., B 90 (2012) 197–203.

[48] Y.H. Li, Q.J. Du, T.H. Liu, X.J. Peng, J.J. Wang, J.K. Sun, Y.H. Wang, S.L. Wu, Z.H. Wang, Y.Z. Xia, L.H. Xia, Comparative study of methylene blue dye adsorption onto activated carbon, graphene oxide, and carbon nanotubes, Chem. Eng. Res. Des. 91 (2013) 361–368.

[49] M.A. Zayed, F.A.N. El-Dien, G.G. Mohamed, N.E.A. El-Gamel, FTIR, magnetic, mass spectral, XRD and thermal studies of metal chelates of tenoxicam, J. Mol. Struct. 841 (2007) 41–50.

[50] J.H. Wang, S.R. Zheng, Y. Shao, J.L. Liu, Z.Y. Xu, D.Q. Zhu, Amino-functionalized $Fe_3O_4@SiO_2$ core-shell magnetic nanomaterial as a novel adsorbent for aqueous heavy metals removal, J. Colloid Interface Sci. 349 (2010) 293–299.

[51] M.V. Reddy, T. Yu, C.H. Sow, Z.X. Shen, C.T. Lim, G.V.S. Rao, B.V.R. Chowdari, Alpha-Fe_2O_3 nanoflakes as an anode material for Li-ion batteries, Adv. Funct. Mater. 17 (2007) 2792–2799.

[52] E. Groppo, C. Lamberti, S. Bordiga, G. Spoto, A. Zecchina, The structure of active centers and the ethylene polymerization mechanism on the Cr/SiO_2 catalyst: a frontier for the characterization methods, Chem. Rev. 105 (2005) 115–183.

[53] D.L.A. deFaria, S.V. Silva, M.T. deOliveira, Raman microspectroscopy of some iron oxides and oxyhydroxides, J. Raman Spectrosc. 28 (1997) 873–878.

[54] W.H. Wang, W. Zhang, H.B. Sun, Q.Y. Du, J.H. Bai, X.L. Ge, C.F. Li, Enhanced photodynamic efficiency of methylene blue with controlled aggregation state in silica-methylene bule-acetate@tannic acid-iron(III) ions complexes, Dyes Pigments 160 (2019) 663–670.

[55] Q.A. Hu, X.R. Zeng, M.W. Fu, Invar effects of $(Fe_{71.2}B_{24}Y_{4.8})_{96}Nb_4$ alloy in different structural states, Appl. Phys. Lett. 97 (2010), 221907.

[56] Z.K. Xiong, B. Lai, P. Yang, Y.X. Zhou, J.L. Wang, S.P. Fang, Comparative study on the reactivity of Fe/Cu bimetallic particles and zero valent iron (ZVI) under different conditions of N-2, air or without aeration, J. Hazard. Mater. 297 (2015) 261–268.

[57] B. Sarac, Y.P. Ivanov, A. Chuvilin, T. Schoberl, M. Stoica, Z.L. Zhang, J. Eckert, Origin of large plasticity and multiscale effects in iron-based metallic glasses, Nat. Commun. 9 (2018) 1333.

[58] W.M. Yang, J.T. Huo, H.S. Liu, J.W. Li, L.J. Song, Q. Li, L. Xue, B.L. Shen, A. Inoue, Extraordinary magnetocaloric effect of Fe-based bulk glassy rods by combining fluxing treatment and J-quenching technique, J. Alloys Compd. 684 (2016) 29–33.

[59] X.C. Sun, A. Cabral-Prieto, M.J. Yacaman, J. Reyes-Gasga, R. Hernandez-Reyes, A. Morales, W.S. Sun, Nanocrystallization behavior and magnetic properties of amorphous $Fe_{78}Si_9B_{13}$ ribbons, Physica B 291 (2000) 173–179.

[60] X.C. Sun, J. Reyes-Gasga, N. Nava, W.S. Sun, Nanocrystallization process and ferromagnetic properties of amorphous $(Fe_{0.99}Mo_{0.01})_{78}Si_9B_{13}$ ribbons, Curr. Appl. Phys. 2 (2002) 187–191.

[61] Y. Tang, Y. Shao, N. Chen, K.F. Yao, Rapid decomposition of Direct Blue 6 in neutral solution by Fe-B amorphous alloys, RSC Adv. 5 (2015) 6215–6221.

[62] D. Musser, C.L. Chien, F.E. Luborsky, J.L. Walter, Influence of carbon on the hyperfine interaction and curie temperatures of amorphous $Fe_{84}B_{16-x}C_x$, J. Appl. Phys. 50 (1979) 1571–1573.

[63] K. Inomata, M. Hasegawa, T. Kobayashi, T. Sawa, Magnetostriction and magnetic core loss at high-frequency in amorphous Fe-Nb-Si-B alloys, J. Appl. Phys. 54 (1983) 6553–6557.